AGU PUBLICATIONS

JGR

Journal of Geophysical Research: Space Physics

RESEARCH ARTICLE

10.1002/2014JA019951

Key Points:
- A pair of strong FACs emerges with opposite polarity to DPY FACs
- Obvious sunward plasma flow channel persists during the period
- Enhanced air densities are found in the cusp region

Correspondence to:
H. Wang,
h.wang@whu.edu.cn

Citation:
Wang, H., H. Lühr, J.-H. Shue, H. U. Frey, G. Kervalishvili, T. Huang, X. Cao, G. Pi, and A. J. Ridley (2014), Strong ionospheric field-aligned currents for radial interplanetary magnetic fields, *J. Geophys. Res. Space Physics*, *119*, 3979–3995, doi:10.1002/2014JA019951.

Received 7 MAR 2014
Accepted 27 APR 2014
Accepted article online 2 MAY 2014
Published online 21 MAY 2014

Strong ionospheric field-aligned currents for radial interplanetary magnetic fields

Hui Wang[1,2], Hermann Lühr[3], Jih-Hong Shue[4], Harald. U. Frey[5], Guram Kervalishvili[3], Tao Huang[1], Xue Cao[1], Gilbert Pi[4], and Aaron J. Ridley[6]

[1]Department of Space Physics, School of Electronic Informatics, Wuhan University, Wuhan, China, [2]Sate Key Laboratory of Space Weather, Chinese Academy of Sciences, Beijing, China, [3]Helmholtz Centre Potsdam, German Research Center for Geosciences, Potsdam, Germany, [4]Institute of Space Science, National Central University, Jhongli, Taiwan, [5]Space Sciences Laboratory, University of California, Berkeley, California, USA, [6]Department of Atmospheric, Oceanic, and Space Sciences, University of Michigan, Ann Arbor, Michigan, USA

Abstract The present work has investigated the configuration of field-aligned currents (FACs) during a long period of radial interplanetary magnetic field (IMF) on 19 May 2002 by using high-resolution and precise vector magnetic field measurements of CHAMP satellite. During the interest period IMF B_y and B_z are weakly positive and B_x keeps pointing to the Earth for almost 10 h. The geomagnetic indices *Dst* is about −40 nT and *AE* about 100 nT on average. The cross polar cap potential calculated from Assimilative Mapping of Ionospheric Electrodynamics and derived from DMSP observations have average values of 10–20 kV. Obvious hemispheric differences are shown in the configurations of FACs on the dayside and nightside. At the south pole FACs diminish in intensity to magnitudes of about 0.1 μA/m^2, the plasma convection maintains two-cell flow pattern, and the thermospheric density is quite low. However, there are obvious activities in the northern cusp region. One pair of FACs with a downward leg toward the pole and upward leg on the equatorward side emerge in the northern cusp region, exhibiting opposite polarity to FACs typical for duskward IMF orientation. An obvious sunward plasma flow channel persists during the whole period. These ionospheric features might be manifestations of an efficient magnetic reconnection process occurring in the northern magnetospheric flanks at high latitude. The enhanced ionospheric current systems might deposit large amount of Joule heating into the thermosphere. The air densities in the cusp region get enhanced and subsequently propagate equatorward on the dayside. Although geomagnetic indices during the radial IMF indicate low-level activity, the present study demonstrates that there are prevailing energy inputs from the magnetosphere to both the ionosphere and thermosphere in the northern polar cusp region.

1. Introduction

The typical interplanetary magnetic field (IMF) is directed on average about 45° away from the solar wind velocity of 400 km/s near the Earth's orbit [e.g., *Parker*, 1958]. The radial IMF, when the IMF is aligned (parallel or antiparallel) with the solar wind velocity, is usually formed in the trailing region of an ICME (interplanetary coronal mass ejection) [e.g., *Neugebauer and Goldstein*, 1997; *Watari et al.*, 2005].

Recent studies have disclosed that both the bow shock and magnetosphere are disturbed during radial IMF periods. The subsolar bow shock locates closer to the Earth during the radial IMF [*Verigin et al.*, 2001], which is overestimated by bow shock models [*Dmitriev et al.*, 2003]. The total dynamic pressure is reduced in the magnetosheath, which is applied to the magnetopause [*Fairfield et al.*, 1990; *Suvorova et al.*, 2010]. As a consequence the magnetopause can expand outward, resulting in the formation of a thin magnetosheath [*Merka et al.*, 2003].

During radial IMF periods the foreshock regions contain multiple types of waves and fluctuations because the reflected particles can interact with the incident solar wind [*Omidi et al.*, 2009], which result in non-stationary and reformed bow shocks [*Lin and Wang*, 2005]. Due to these local ripples on the bow shock, transient flux enhancements or high kinetic energy jets will occur in the magnetosheath [e.g., *Němeček et al.*, 1998; *Shue et al.*, 2009; *Hietala et al.*, 2009]. If the jet speed is supersonic, a secondary shock can form near the magnetopause [*Hietala et al.*, 2009]. These jets can cause large perturbations on the magnetopause [e.g., *Hietala et al.*, 2009; *Amata et al.*, 2011], even causing sunward flows [*Shue et al.*, 2009]. The magnetopause is

unsteady and oscillates with a period of a few minutes [e.g., *Fairfield et al.*, 1990; *Russell et al.*, 1997; *Němeček et al.*, 1998; *Merka et al.*, 2003].

Recent work has shown that magnetosheath jets can cause short-lived ionospheric sunward flow channels in the cusp region [*Hietala et al.*, 2012]. However, *Farrugia et al.* [2007] have reported generally a calm magnetosphere (weak convection and no substorm activity) with weak dayside reconnection at low and high latitudes during radial IMF periods. Based on model simulation, *Tang et al.* [2013] have shown that magnetic reconnection can exist at the equatorward boundary of the cusp in one hemisphere while on the poleward boundary of the cusp in the other hemisphere, and Kelvin-Helmholtz instability can be excited on both flanks of the magnetosphere.

Quite few works have focused on the response of the ionosphere and thermosphere to radial IMF. Field-aligned currents (FACs) play an important role in the coupling processes of the electromagnetic energy between the solar wind, magnetosphere, and ionosphere. It has been long recognized that the characteristics of large-scale FACs are controlled by solar wind and IMF conditions [e.g., *Feldshtein and Levitin*, 1986; *Lu et al.*, 1995a; *Stauning*, 2002; *Wang et al.*, 2005; *Nenovski*, 2009; *Green et al.*, 2009; *Juusola et al.*, 2009; *Gjerloev et al.*, 2011; *Li et al.*, 2011]. Various models of FACs have been constructed under various IMF and solar wind conditions [e.g., *Weimer*, 2001; *Papitashvili and Rich*, 2002; *He et al.*, 2012].

There were mainly four types of FACs revealed in the past, e.g., Region 1 (R1), Region 2 (R2), northward IMF B_z (NBZ), and IMF B_y modulated (DPY) FACs [e.g., *Iijima and Potemra*, 1976; *Iijima et al.*, 1984; *Potemra et al.*, 1987]. R1 FACs flow into the ionosphere in the morning sector and out of the ionosphere in the evening sector, and R2 FACs are located equatorward of the R1 FACs with opposite polarities. When IMF B_z is pointing northward, NBZ FACs dominate in the polar cap poleward of R1 FACs [*Iijima et al.*, 1984]. The NBZ FACs have been interpreted in terms of the antiparallel reconnection on field lines tailward of the dayside cusp [e.g., *Crooker*, 1988; *Iijima et al.*, 1984; *Wang et al.*, 2008a]. When IMF B_y becomes dominant DPY FACs form around the noon sector [e.g., *Iijima and Potemra*, 1976; *Wilhjelm et al.*, 1978; *Clauer and Friis-Christensen*, 1988]. When B_y is positive, in the Northern Hemisphere the upward field-aligned current is located poleward of the downward current, and vice versa in the Southern Hemisphere. The poleward part of DPY currents could be associated with the plasma mantle/cusp precipitation, while the equatorward part is an intrusion of dawnside ($B_y > 0$) or duskside ($B_y < 0$) R1 currents [e.g., *McDiarmid et al.*, 1979; *Friis-Christensen et al.*, 1985; *Erlandson et al.*, 1988; *Wing et al.*, 2010], or some (even all) of the equatorward parts originate from the cusp/mantle region [e.g., *Taguchi et al.*, 1993; *Mei et al.*, 1994; *Yamauchi et al.*, 1993; *Xu and Kivelson*, 1994; *Watanabe et al.*, 1996; *Haraguchi et al.*, 2004; *Wang et al.*, 2008a].

The high-latitude ionospheric convection pattern strongly depends on the orientation of IMF [*Heelis et al.*, 1984, and references therein]. Normally, for southward IMF two-cell convection flow pattern exists, while for northward IMF four-cell flow pattern emerges due to high-latitude reconnection. IMF B_y will distort the convection map and cause dawn-dusk and interhemispheric asymmetries. The location of the auroral oval and its activity have been found to strongly depend on the IMF configuration [*Holzworth and Meng*, 1975, and references therein]. *Shue et al.* [2002] have found that the north auroral power is higher when all IMF components are negative. *Yang et al.* [2013] have concluded that the dayside aurora are brighter for $B_x < 0$ than for $B_x > 0$ during southward IMF, while nightside aurora brightness is less dependent on IMF B_x, and the duskside auroral brightness for northward IMF is not so much brighter for $B_x < 0$ than for $B_x > 0$. The thermospheric air density is important in understanding the thermosphere-ionosphere coupling process. The dynamics of the high-latitude thermosphere is greatly affected by the energy input from the solar wind via Joule heating and particle precipitation [*Lühr et al.*, 2004; *Strangeway et al.*, 2005, and references therein].

Few works have concentrated on the configuration of FACs, ionospheric convection, aurora activity, and thermospheric neutral mass density in response to radial IMF. In the present work we aim to investigate the event on 19 May 2002, which is featured as a long period with steady solar wind and radial IMF, with special attention to the responses of both the ionosphere and thermosphere. In the following section we briefly describe the method of data processing. Section 3 describes the observational results. In the discussion section we compare results with previous reports and offer explanations.

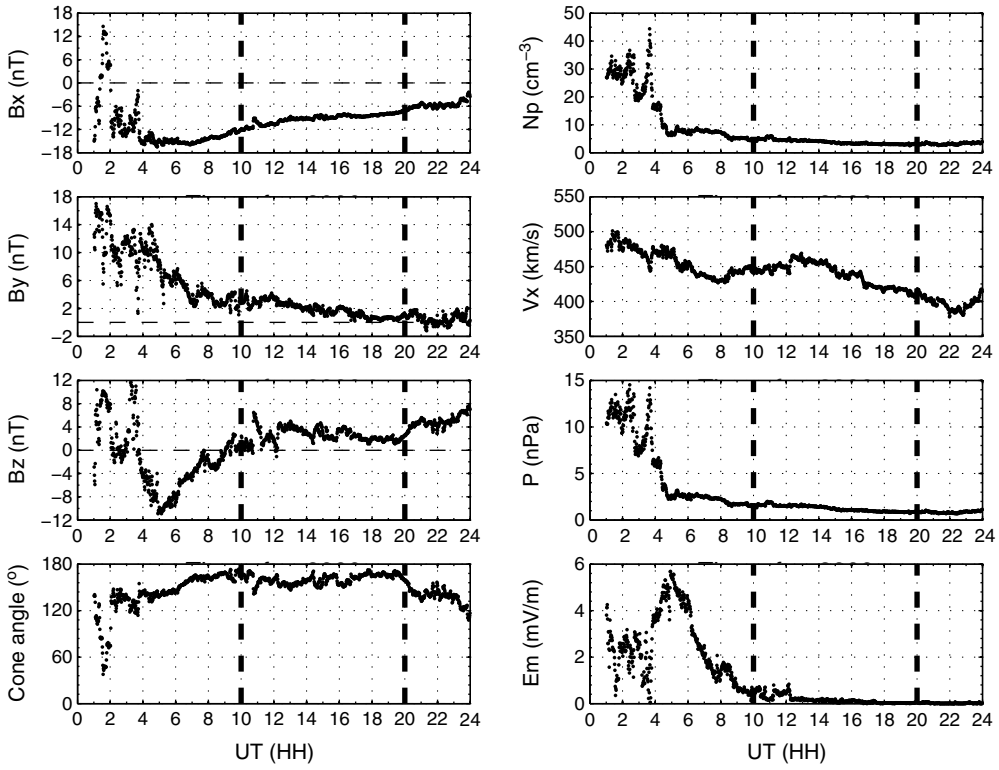

Figure 1. The solar wind parameters observed by ACE including IMF B_x, B_y, and B_z components in GSM coordinates, the cone angle, density N_p, velocity v_x, dynamic pressure P, and merging electric field E_m. The cone angle is defined as $\arccos(B_x/B_T)$, where B_T is the total magnetic field strength. On 19 May 2002 we find typical radial IMF conditions. The parameters have been time shifted to the magnetopause.

2. Data Sets

2.1. CHAMP Orbit and Observation

CHAMP has a near-polar (83.7° inclination) orbit with an initial altitude of ~450 km [*Reigber et al.*, 2002]. During 2002 and 2003 the altitude decreases to ~ 400 km on average. The orbit covers all local times within 130 days (~4 months). During the times of interest the CHAMP satellite is approximately in the noon-midnight meridian (13–01 magnetic local time (MLT) sector), thus enabling us to study the dayside and nightside dynamics of large-scale FACs. CHAMP carries a fluxgate magnetometer (FGM), which delivers vector field readings at a rate of 50 Hz and a resolution of 0.1 nT. The data are calibrated with respect to the onboard absolute scalar overhause magnetometer. The orientation of field vectors are provided by a dual-head star camera system mounted together with the FGM on an optical bench. Data used in this study are the 1 Hz preprocessed vector data in the North-East-Center frame.

The FAC density is determined according to Ampere's law from the vector magnetic field data by solving the curl-B, that is, $j_z = \frac{1}{\mu_0}\left(\frac{\partial B_y}{\partial x} - \frac{\partial B_x}{\partial y}\right)$, where μ_0 is the vacuum permeability, B_x and B_y are the transverse magnetic field deflections caused by the currents. We have assumed that FACs are infinite sheets aligned with the mean location of the auroral oval [*Wang et al.*, 2005]. Since we do not have multipoint measurements, we convert spatial gradients into temporal variations by considering the velocity under the assumption of the stationary of the current during the time of satellite passage. After discrete sampling is introduced [*Lühr et al.*, 1996], we obtain $j_z = \frac{1}{\mu_0 v_x}\frac{\Delta B_y}{\Delta t}$, where v_x is the velocity perpendicular to the current sheet and B_y is the magnetic deflection component parallel to the sheet.

CHAMP has a STAR (Space Three-axis Accelerometer for Research) mission accelerometer on board, from which the thermospheric mass density can be derived by using a new algorithm [*Doornbos et al.*, 2010]. The air density has been normalized to an altitude of 400 km. The accuracy of the air density measurement has been improved over previous work to about 5×10^{-14} kg/m^3.

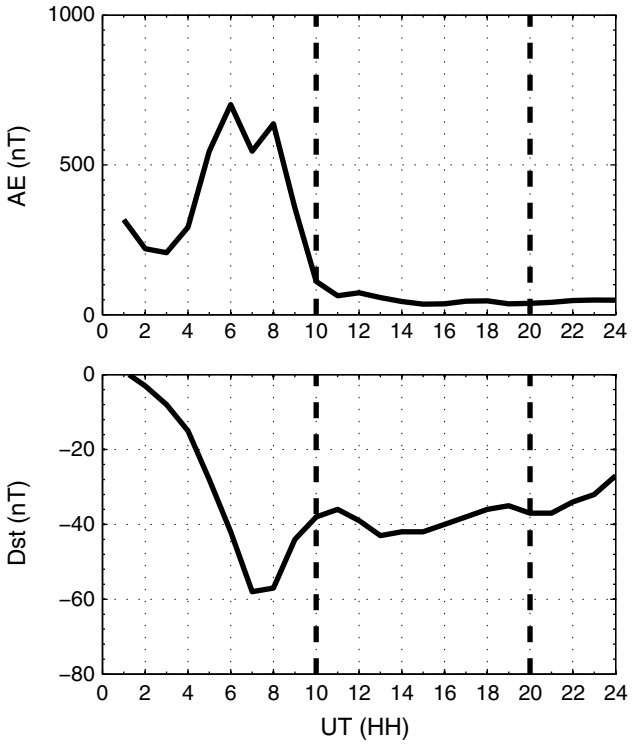

Figure 2. Geomagnetic activity conditions on 19 May 2002: *AE* and *DST* indices during radial IMF conditions (bracketed by vertical dashed lines).

Only those CHAMP passes are selected for analysis where the angle between the orbital track and the auroral oval is greater than 45°. This is to guarantee that the CHAMP cross-track direction is approximately aligned with the auroral oval. The data are all presented in the Apex magnetic coordinate system [e.g., *Richmond*, 1995].

2.2. DMSP Orbit and Observation

The DMSP orbital period is approximately 100 min, and the altitude is ~835 km. The satellites have fixed local times with F13 in the near dawn-dusk sector and F15 in the dayside-nightside (09–22 MLT) local time sector. The ion drift meter (IDM) can provide ion drift velocities in both horizontal and vertical directions perpendicular to the satellite orbit [*Rich and Hairston*, 1994]. The along-track potential, Φ, can be derived as

$$\Phi = \int (-\vec{V}\times\vec{B})\mathrm{d}s = \int (-V_y B_z + V_z B_y)\mathrm{d}x, \quad (1)$$

where $\vec{V}$ is the cross-track plasma velocity, $\vec{B}$ is the geomagnetic field, x is the component along the satellite path, z is radially away from the center of the Earth. The International Geomagnetic Reference Field magnetic field model is used as the $\vec{B}$ field. The average energy flux of electrons and ions in the range of 30 eV to 30 keV are monitored by the DMSP electron spectrometer Special Sensor Precipitating Electron and Ion Spectrometer (SSJ/4) instruments [*Hardy et al.*, 1984]. We use an empirical relationship between the average electron energy flux and the height-integrated ionospheric conductivity [*Robinson et al.*, 1987] to determine the poleward boundary of the auroral region. For that we first calculate the auroral Pedersen conductance along the DMSP path and find the peak in conductance, then stepping poleward until the conductance is reduced to 0.2 times the peak value. A similar method has been used to determine the equatorward boundary of the auroral oval [e.g., *Wang et al.*, 2008b].

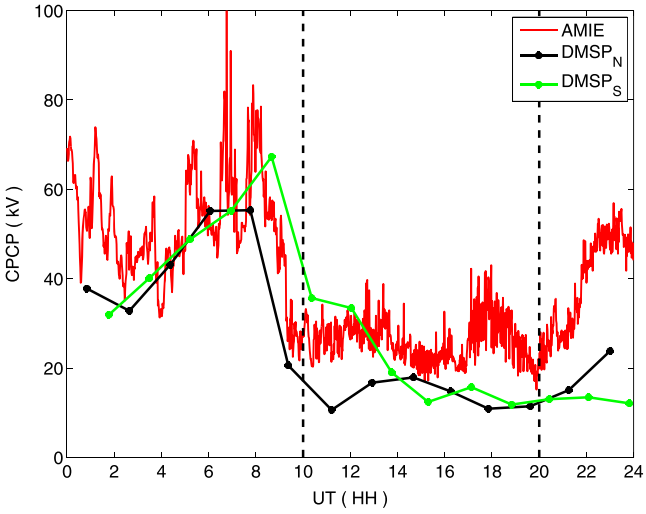

Figure 3. The diurnal variation of the ionospheric cross polar cap potential from AMIE (red) and from DMSP observations (black is for the north pole and green for the south).

2.3. AMIE-Derived CPCP Data

The Assimilative Mapping of Ionospheric Electrodynamics (AMIE) technique is used extensively in the scientific community, which has been employed to predict the high-latitude cross polar cap potential (CPCP) at 1 min resolution, which is the total potential difference (maximum potential minus minimum potential). The global magnetometer data, the available

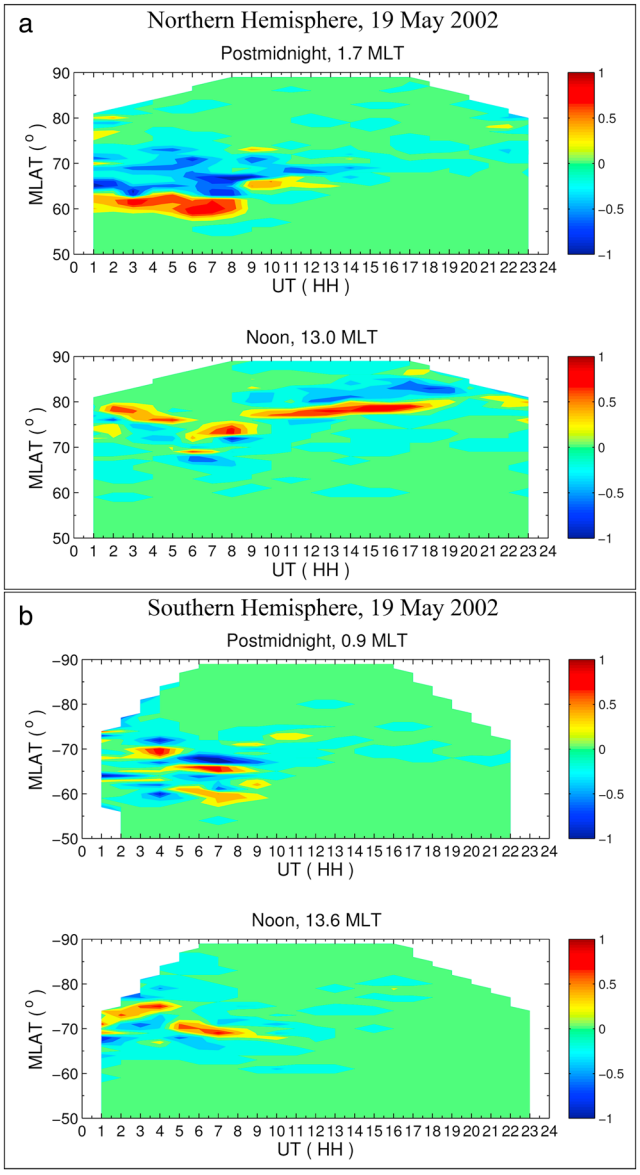

Figure 4. Latitudinal versus diurnal variations of FACs observed by CHAMP on the (top) nighttime and (bottom) daytime in the (a) Northern and (b) Southern Hemispheres. Current densities are given in μA/m^2. FAC density above 1 μA/m^2 go into saturation. Positive values represent upward FACs.

IMF, solar wind, HPI (hemispheric power index), $F_{10.7}$, and *DST* data are used as inputs into the AMIE model [*Ridley et al.*, 2004]. The advantages of AMIE are stated by comparing AMIE to other models [*Ridley*, 2005].

3. Observations

3.1. Solar Wind and IMF

Figure 1 shows the time history of 1 min time resolution solar wind inputs on 19 May 2002 observed by the ACE spacecraft. The data have been time shifted to the dayside magnetopause. Figure 1 (left) contains the components of IMF B_x, B_y, and B_z in GSM coordinates and the cone angle defined as arccos $\frac{B_x}{B_T}$, where B_T is the magnitude of the magnetic field. When IMF is purely directed to the Sun (Earth), the cone angle reaches a value of 0° (180°). In Figure 1 (right) we can see the solar wind velocity, v_{sw}, density, N_p, dynamic pressure, P_d, and merging electric field, $E_m = v_{sw}\sqrt{B_y^2 + B_z^2}\sin^2(\theta/2)$, where the clock angle, θ, is the angle of the IMF in the GSM y-z plane with respect to the $+z$ direction [*Kan and Lee*, 1979].

There is a southward turning of the IMF B_z at ~ 3.5 UT (universal time) with a minimum value of −10.9 nT around 5 UT. B_z turns northward around 10 UT and has an average value of 2.7 nT. The duskward B_y has an average magnitude of 1.7 nT after 10 UT. The negative B_x component approaches a minimum of about −16 nT around 4–6 UT and changes to an average value of −8.8 nT in the remaining hours. It is apparent that the B_x component is dominant after 10 UT with a cone angle of about 160°. The Alfvénic Mach number is 4.3 during the dominant radial IMF period, which is smaller than the nominal value of 8 (not shown in the figure). The dynamic pressure drops around 4.5 UT due to the decrease of the solar wind density. After 4.5 UT the dynamic pressure has no obvious variations and stays at a constant value of about 1 nPa. The merging electric field attains a peak around 4.5 UT. The interesting period of the quasi-radial IMF interval lasts for about 10 h from 10 to 20 UT.

The diurnal variations of geomagnetic indices are shown for reference in Figure 2. The *DST* index approaches a minimum value of −59 nT at 7 UT, recovers gradually to −40 nT after 10 UT. The weak storm occurs apparently after a southward turning of the IMF (see Figure 1). The *AE* index attains peaks of about 700 nT between 6 and 8 UT and remains at a value 100 nT after 10 UT. Aside from a long recovery of *DST* from the early activity (−59 nT), the geomagnetic indices show steady and low-level activity. Thus, it can be said that the geomagnetic activity is at low levels during the interval of radial IMF.

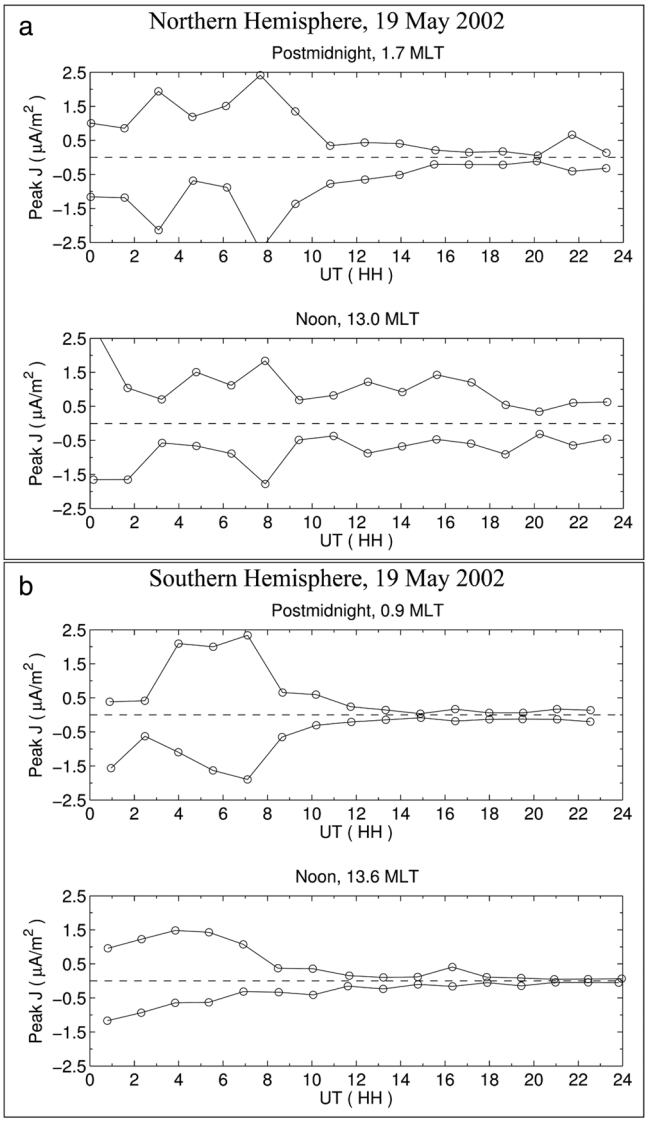

Figure 5. The diurnal variation of peak densities of FACs observed by CHAMP on the (top) nighttime and (bottom) daytime in the (a) Northern and (b) Southern Hemispheres.

3.2. AMIE and DMSP CPCP

The diurnal variation of CPCP predicted by AMIE and derived from DMSP measurements in both hemispheres are shown in Figure 3. It can be seen that the modeled CPCP drops to 20 kV around 10 UT. The observed southern storm time CPCP peak is larger and recovers at a later time than in the north. The CPCP value decreases to 10 kV around 11 (13.5) UT in the Northern (Southern) Hemisphere.

3.3. CHAMP FACs

Figure 4 shows the color-coded distribution of FAC density as a function of MLAT (magnetic latitude) versus UT, as observed by CHAMP satellite. Separate frames are used for the dayside and nightside in both hemispheres. White areas represent uncovered areas. Downward FACs are shown in blue and upward in red. FACs densities get enhanced during the storm period, and the equatorward and poleward shifts of intense FACs are well correlated with the storm expansion and recovery periods, which is more obvious on the dayside than on the nightside. These storm time characteristics of FACs have been reported previously [e.g., *Bythrow et al.*, 1984; *Fujii et al.*, 1992; *Anderson et al.*, 2002; *Wang et al.*, 2006].

When looking at the FACs density during the radial IMF period from 10 to 20 UT, there are obvious dayside-nightside differences in the Northern Hemisphere. On the nightside the intense FACs occur only during the storm periods, then decrease during the storm recovery phase. During the period of radial IMF, FACs intensity becomes quite weak. However, on the dayside an intense two-sheet FACs configuration emerges (downward in the poleward and upward in the equatorward) during the radial IMF period with the centers shifting poleward. This pair of FACs has an opposite direction to DPY FACs for duskward IMF, and IMF B_y is quite weak for this case. In the Southern Hemisphere both the dayside and nightside FACs become weak during the radial IMF period.

The peak current densities of both upward and downward FACs are shown in Figure 5 as a function of UT. It is obvious in the Northern Hemisphere, on the dayside both the upward and downward FACs are strong from 10 to 20 UT with magnitudes of around 1 $\mu A/m^2$, which are quite comparable to the early storm time strength, while on the nightside FACs drop in magnitude to about 0.2 $\mu A/m^2$ around 10 UT. In the Southern Hemisphere on the day and nightside, FACs become weak with values of about 0.1 $\mu A/m^2$ around 10 UT.

3.4. Neutral Air Density

According to previous work [*Lühr et al.*, 2004], intense cusp FACs can dump energy into the thermosphere, and cause the upwelling of neutral air. Thus, it might be interesting to examine the spatial and temporal variation of the accompanying air density, which is shown in Figure 6 in the same format as Figure 4. The air

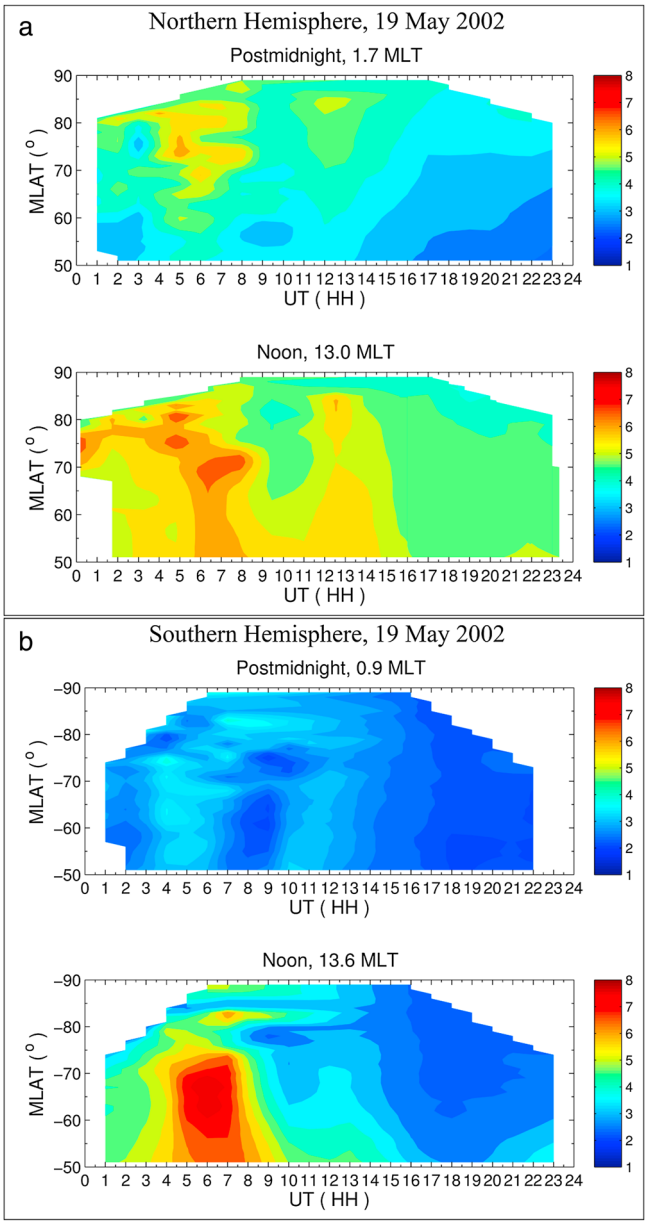

Figure 6. Latitudinal versus diurnal variations of air density observed by CHAMP on the (top) nighttime and (bottom) daytime in the (a) Northern and (b) Southern Hemispheres. Air densities are given in $10^{-12} kg/m^3$.

density is generally larger on the dayside than on the nightside in both hemispheres. It is interesting to see that there are two periods showing enhanced air densities, one during the storm period with a peak value of about 7×10^{-12}kg/m^3 and the other during the radial IMF period with a peak value of about 6×10^{-12}kg/m^3 around 12 UT. In the Southern Hemisphere we find enhanced air density only during the storm main phase on the dayside, while on the nightside the air density is generally quite low for the whole day.

3.5. Plasma Flow

Ionospheric plasma convection observed by DMSP F13 in the dawn-dusk sector is shown in Figure 7. Positive (red color) denotes sunward flows. Overplotted is the derived poleward boundary of the auroral oval from the SSJ4 particle data, as denoted by black circles. The hollow circle is for F13 and the solid for F15. Due to data missing the oval boundaries are not continuous. In general, there are two cells of plasma flow, with sunward flow (positive value) in both the auroral zones, and antisunward flow (negative value) in the polar cap. Interestingly, in the northern polar cap there are weak sunward flows (positive value) occurring at higher latitudes near the north pole after 10 UT when the IMF is weakly northward. No such features appear in the southern polar cap. The high-latitude sunward flow reaches a maximum of about 700 m/s around 12 UT when looking closely at single orbit segments.

3.6. Auroral Observations

The Thermosphere Ionosphere Mesosphere Energetics Dynamics (TIMED) satellite is in a circular orbit with 71.4° inclination and a period of 1.7 h at an altitude of 625 km. Global Ultraviolet Imager (GUVI) on board of TIMED provides accumulated aurora observations over about 20 min. It scans aurora images in a relatively narrow sector as compared to the IMAGE satellite, on the day of our event mainly in the Northern Hemisphere duskside and Southern dawnside from 0323 to 0726 UT. The IMAGE satellite is in a highly eccentric polar orbit of 1000 × 45,600 km altitude. The WIC (Wideband Imaging Camera) on board IMAGE provides observations of the northern aurora at wavelengths of 140–180 nm on a global scale with a spatial resolution of 50 km and a temporal resolution of 2 min. The satellite goes through perigee between 1000 and 1400 UT, and the instrument is turned off. Toward the end the view get smaller as the spacecraft gets closer to Earth and one can not see the whole oval anymore.

Figures 8 and 9 show auroral images from TIMED GUVI and Imager for Magnetopause-to-Aurora Global Exploration (IMAGE) WIC in the frame of MLAT and MLT coordinates. The coordinate frame used to order

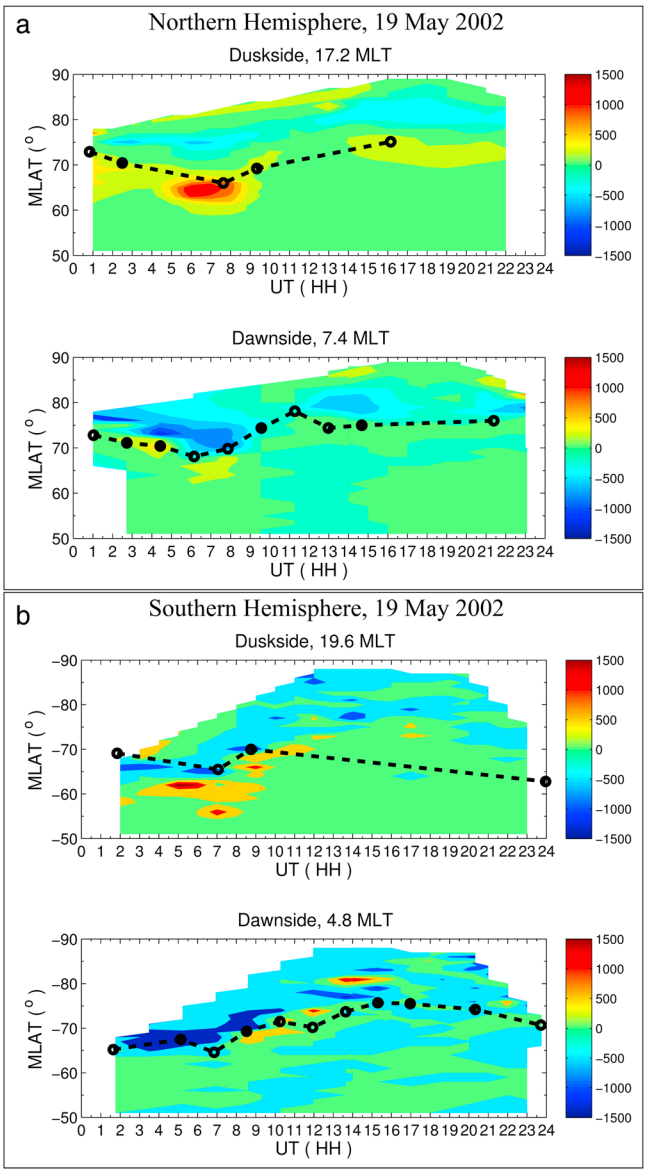

Figure 7. Latitudinal and diurnal variations of azimuthal plasma flow observed by DMSP F13 on the (top) duskside and (bottom) dawnside in the (a) Northern and (b) Southern Hemispheres. Plasma flow velocity is given in m/s. Positive values represent sunward drifts. The poleward boundary of the auroral oval is indicated by black circles. The hollow circle is for F13 and the solid for F15.

the observations is the Apex coordinate system. A weak northern transpolar auroral arc detached from the premidnight aurora is captured at 03:23 UT by GUVI as shown in Figure 8 (top left). This arc becomes more intense when the geomagnetic storm begins, as shown in Figure 8 (bottom left). No transpolar arcs appear in the morning sector of the southern auroral region. GUVI has narrow view of north aurora after 08:14 UT. The observed south aurora is quite weak on 18:42 UT, as shown in Figure 8d.

As observed by IMAGE in Figure 9a the storm time arc structure is mainly confined to the premidnight sector aligned with the oval before 09:00 UT. Afterward the arcs approach the postnoon cusp region (Figures 9b and 9c). After 14:15 UT when IMAGE is turned on again, the aurora becomes rather dim in response to the radial IMF orientation except for the afternoon, where a bright spot of aurora can be noticed, which tends to expand toward the dusk sector (Figure 9d).

In the interval of interest of the radial IMF, there are bright aurora in the northern noontime from IMAGE observations, while the aurora are rather dim in the south pole from GUVI observations, which seems

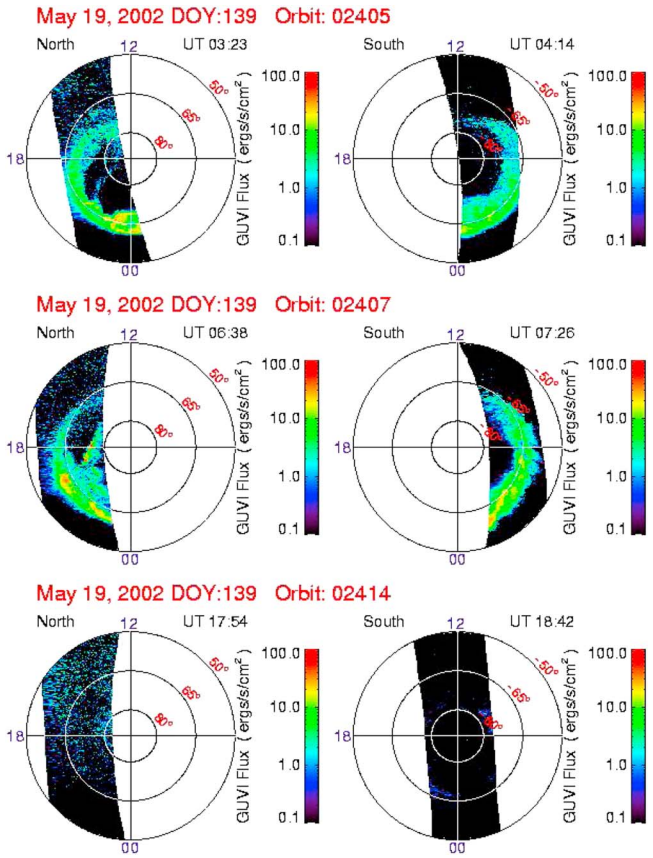

Figure 8. (top to bottom) The auroral images observed by TIMED GUVI in the Northern and Southern Hemispheres. The images in the Figure 8 (bottom) is during radial IMF period.

to be consistent with previous finding that IMF $B_x < 0$ favors more aurora activity in the noontime [*Yang et al.*, 2013].

4. Discussion

We have presented the spatial and temporal variation of ionospheric and thermospheric parameters during radial IMF periods. Interhemispheric and dayside-nightside differences have been shown. In the northern cusp region, pairs of noontime FACs remain as strong as those during the preceding storm time, but they become rather weak in the south. The nigthtime FACs turn weak in both hemispheres. A sunward plasma flow channel persists in the north polar cap, which disappears in the south. The aurora is bright in the northern cusp region, but rather weak in the south. There are enhanced air densities in the northern cusp, but not in the south. All these observations indicate that there are prevailing energy inputs from the magnetosphere to both the ionosphere and thermosphere in the northern cusp region during the radial IMF period, despite the geomagnetic activities are at low levels.

4.1. Sunward Convection

To get a better understanding of the processes occurring in the polar region, successive CHAMP and DMSP orbits from 10 to 20 UT (radial IMF period) have been used to produce the polar view plots for both FACs and plasma flows. Due to the larger separation between the magnetic and geographic poles in the south the satellites cover a wider MLT region in the southern pole region.

Figure 10 shows the MLT and MLAT distribution of the azimuthal and upward flow velocity. The poleward boundary of the auroral oval has been overplotted for reference, as denoted by black asterisks. During these periods sunward flow channels in the ionosphere with velocities of 700 m/s have been found (Figure 10, top), which are not observed in the south pole (Figure 10, middle).

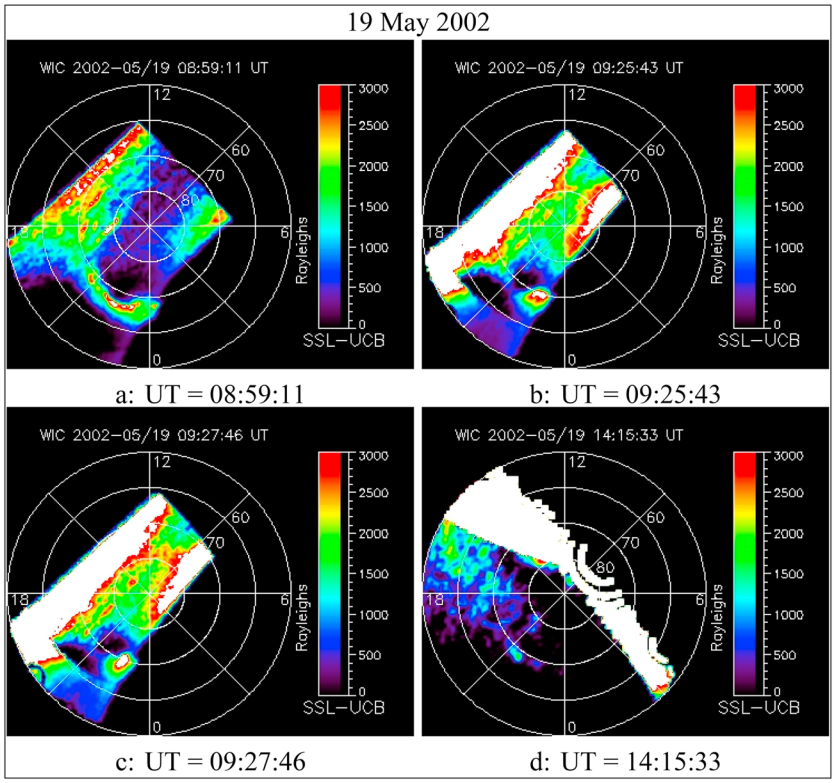

Figure 9. (a–d) North pole auroral images observed by IMAGE WIC. IMAGE is turned off between 10 and 14 UT when passing through perigee. The aurora image around 14 UT is during radial IMF period shown in Figure 9d. The transpolar arcs are emphasized therefore the bright auroras go into saturation (white areas in the images).

To support DMSP observations, Figure 11 shows the northern polar map of ionospheric potential calculated from AMIE in the MLAT and MLT coordinate system, with noon to the top and dusk to the left. The maximum and minimum potentials are shown in the bottom. Contours of constant potential are given in black, with red for positive and blue for negative potential. It is interesting to see that there is a large positive potential emerging in the polar cap around 11:00 UT, indicating an enhanced counterclockwise rotating plasma flow, which is consistent with the DMSP observation that there are obvious sunward flows near the noon-midnight meridian. This positive potential (sunward flow) persists during the whole radial IMF period, as confirmed by AMIE results.

Hietala et al. [2012] have reported that during radial IMF period there are ionospheric sunward jets in the cusp region and associated them with the magnetosheath jets. They have argued that the high dynamic pressure jets in the magnetopause might trigger reconnection events, thus resulting in the ionospheric sunward flows. However, the ionospheric flows reported by them are quite short lived (5 min) and localized, while the sunward flows in the present study last for the whole radial IMF period. The long-lived sunward flow might indicate that there are permanent magnetic reconnections occurring poleward of the polar cusp region, e.g., in the magnetospheric flank. The reconnected field lines then move sunward to the dayside magnetosphere. The lack of effect in the south indicates that the reconnection prefers to occur in the north. According to the antiparallel reconnection paradigm [*Dungey*, 1963], the earthward directed IMF is in opposite direction to the geomagnetic field poleward of the northern cusp region while in the same direction in the southern cusp region. The north-south asymmetry in the lobe reconnection due to IMF has been discussed in previous works [e.g., *Crooker*, 1979; *Cowley*, 1981; *Reiff and Burch*, 1985]. Recent model work has shown that when IMF is purely sunward directed, magnetic reconnection can happen at high latitudes in the southern magnetospheric flanks [e.g., *Tang et al.*, 2013]. Interestingly, large upflows are also observed in the cusp region, as shown in Figure 10 (bottom).

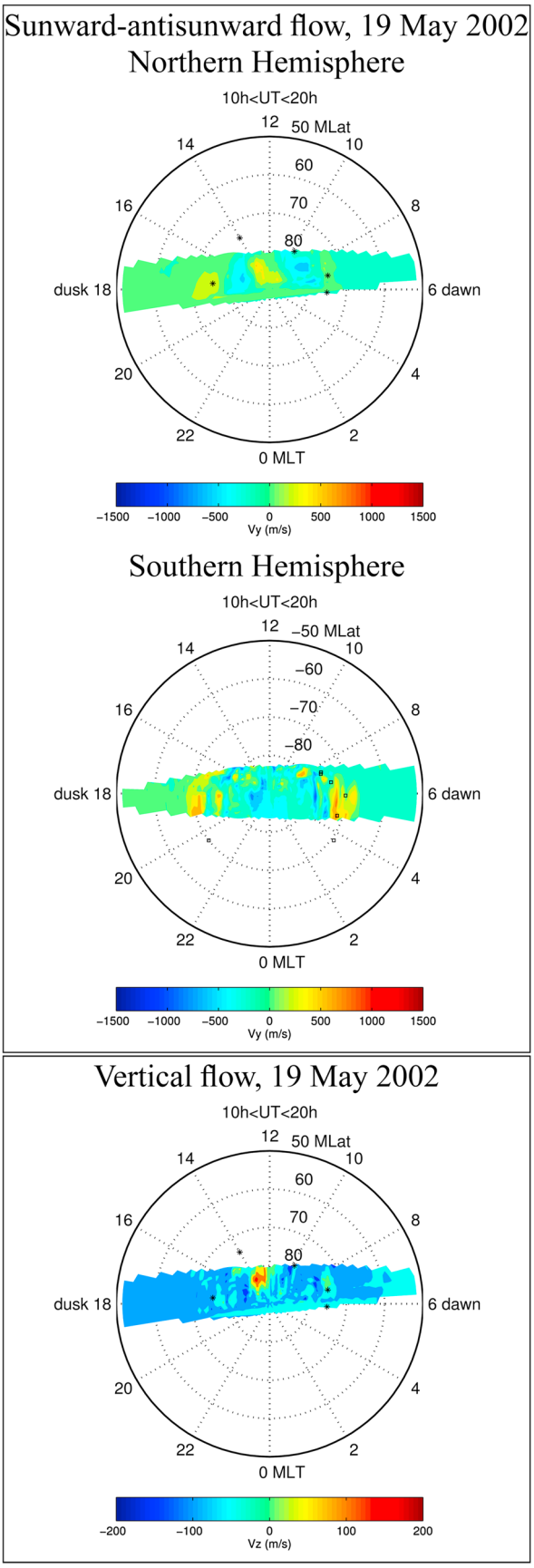

Previous studies from observations and models have shown that smaller Mach Number solar wind is favorable for magnetic reconnection at high latitudes, which allows sunward convection on open field lines in the magnetosphere, as the Lorentz force, $J \times B$, caused by near cusp or flank reconnection can in these cases significantly exceed the magnetosheath dynamic pressure [e.g., *Cassak*, 2011; *Lavraud and Borovsky*, 2008; *Wilder et al.*, 2013; *Eriksson and Rastätter*, 2013]. The Mach Number in our case is relatively low attaining mean values of 4.3 during the radial-dominated period which is favorable for the magnetic reconnection processes to occur.

4.2. FACs and Air Density

When looking at the FACs distribution in the Northern Hemisphere as shown in Figure 12, it can be seen that FAC pairs persist in the polar cusp region, with the downward FACs toward the pole and upward FACs at lower latitude. When examining Figures 10 and 12, it can be noticed that the sunward convection coincides with the FAC region.

The lack of strong FACs and sunward convection flow in the southern polar region confirms the interhemispheric independent response of the high-latitude electrodynamics, and in our case a Northern Hemispheric preference of the high-latitude reconnection process. FACs density may also be affected by the conductivity differences due to solar illumination. The increase in the ionospheric conductivity will enhance the FACs density around noon [e.g., *Fujii and Iijima*, 1987; *Russell and Fleishman*, 2002; *Cattell et al.*, 2003; *Wang et al.*, 2005]. During 10–20 UT, the northern cusp is fully in sunlight, while the southern cusp is partly in sunlight. According to our previous statistical study of the dependence of FACs on the solar illumination during quiet period [*Wang et al.*, 2005], the noontime FACs density in sunlight can be on average 1 $\mu A/m^2$, while in darkness they can be around 0.5 $\mu A/m^2$ [see *Wang et al.*, 2005, Figure 10). However, in the present study, FACs in the southern cusp region drops to 0.1 $\mu A/m^2$ on average, which can not

Figure 10. (top to bottom) Azimuthal and vertical flow on successive polar orbits of DMSP F13 during the radial IMF period from 10 to 20 UT. The poleward boundary of the auroral oval has been overplotted for reference, as denoted by black asterisk.

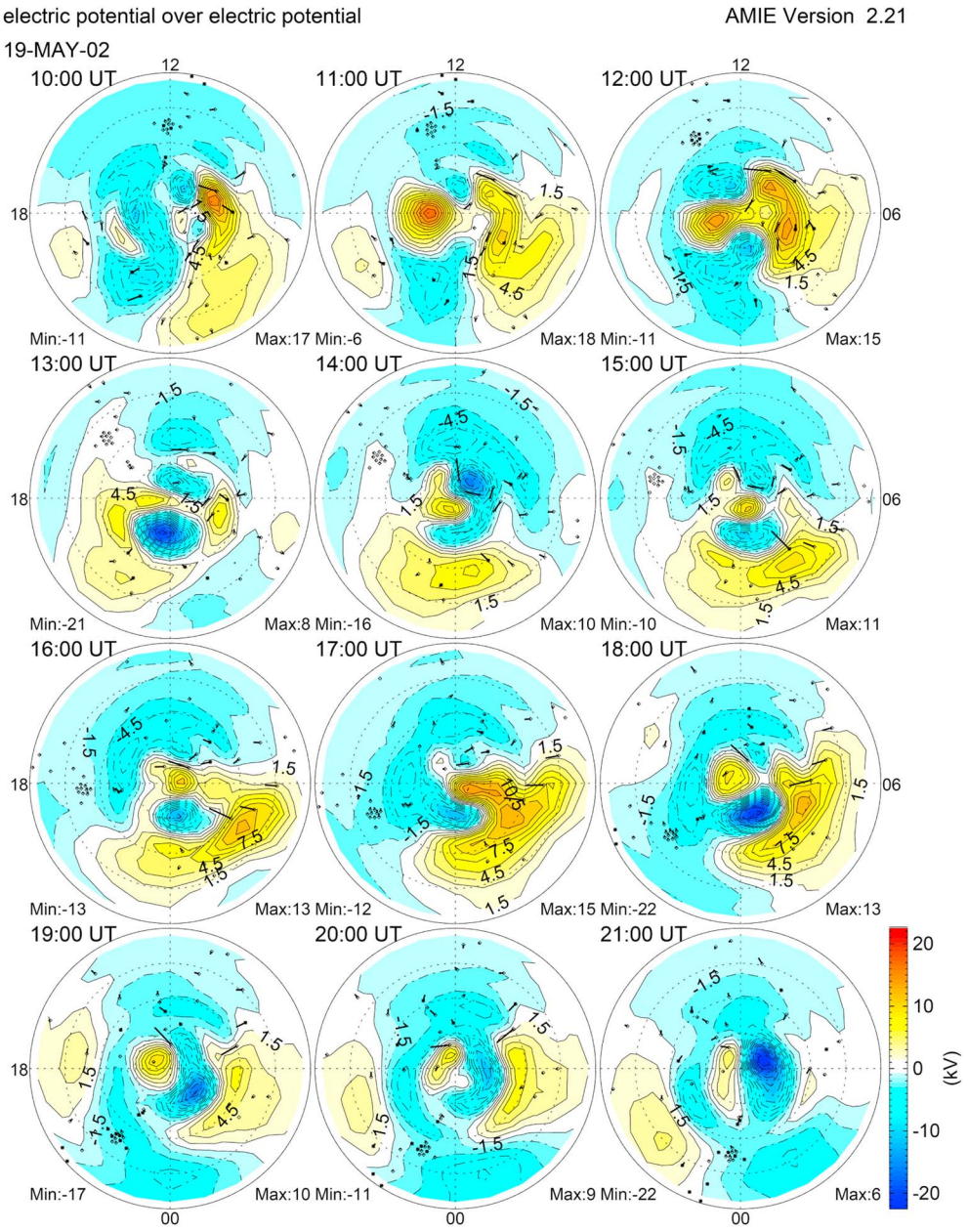

Figure 11. The ionospheric potential (kV) in a magnetic latitude and magnetic local time coordinate system with noon to the top and dusk to the left in the Northern Hemisphere under radial IMF period from AMIE. Contours of constant electric potential are shown in black. Red denotes positive potential (counterclockwise rotation of the plasma flow), and blue denotes negative potential (clockwise rotation of the plasma flow). The outer circle is for 50° MLAT.

be only attributed to the solar illumination effect. The lack of lobe reconnection in the southern magnetospheric flank region could play an important role in causing the low density of FACs.

The air density variation after subtraction of the background is shown in Figure 12 in the MLT-MLAT coordinates for the period from 10 to 20 UT. We find enhanced air densities near the northern cusp region. Previous works have disclosed that during large IMF B_y the upwelling of the neutral gas can occur in the cusp region accompanied by intense FACs, which originate from the reconnection process on the high-latitude magnetospheric flanks [e.g., *Lühr et al.*, 2004; *Eriksson et al.*, 2009; *Crowley et al.*, 2010; *Knipp et al.*, 2011; *Li et al.*, 2011; *Wilder et al.*, 2013; *Kervalishvili and Lühr*, 2014]. The present work has shown that upwelling of neutral air associated with enhanced FACs can also occur during periods of strong radial IMF. The intense FACs and the associated ionospheric current system in the dayside cusp region can cause locally

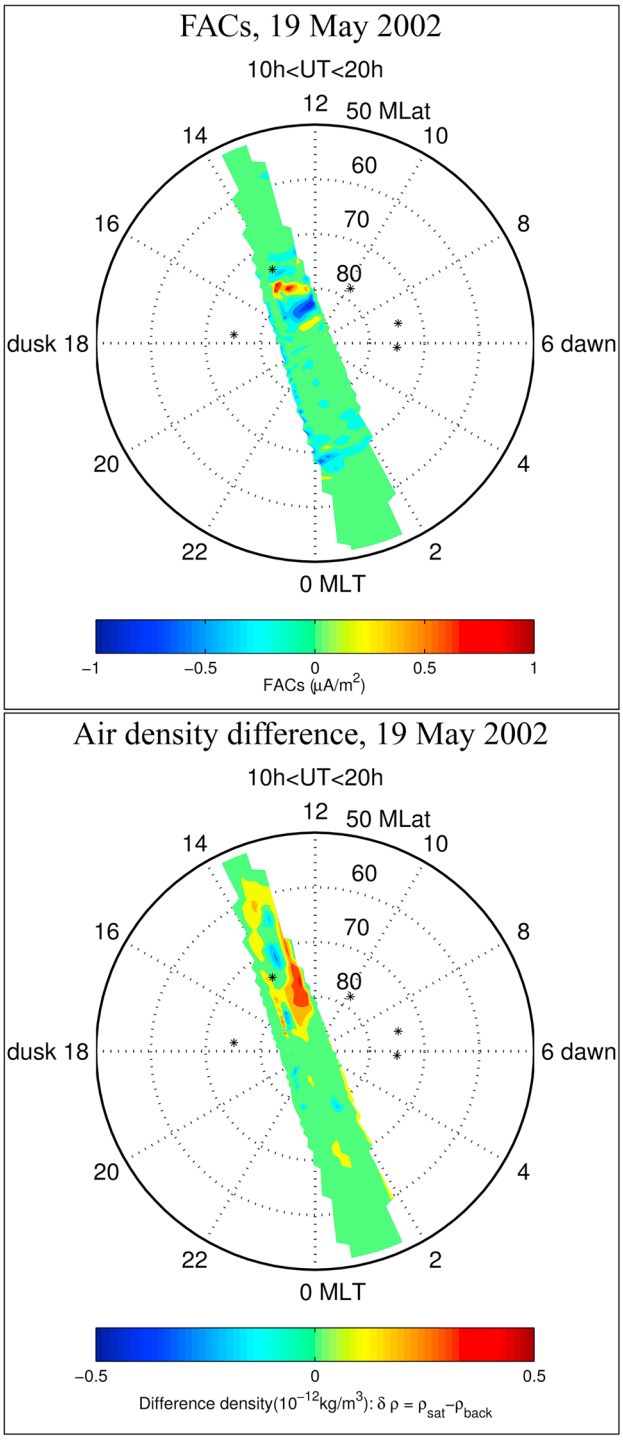

Figure 12. FACs and air density differences after subtraction of the background density along successive polar CHAMP orbits in the Northern Hemisphere during the radial IMF period from 10 to 20 UT. The poleward boundary of the auroral oval has been overplotted for reference, as denoted by black asterisk.

Joule heatings at lower altitude, and the warm air is upwelling resulting in a density enhancement at 400 km and above. Strong plasma upflow coincides with the cusp FACs, which might result from the interaction of the ion-neutral frictional heating (See Figure 10).

Other heating sources of the ionosphere and thermosphere come from Poynting flux and soft electron particle precipitation [e.g., *Strangeway et al.*, 2000, 2005; *Deng et al.*, 2013]. Neutral wind can also affect the

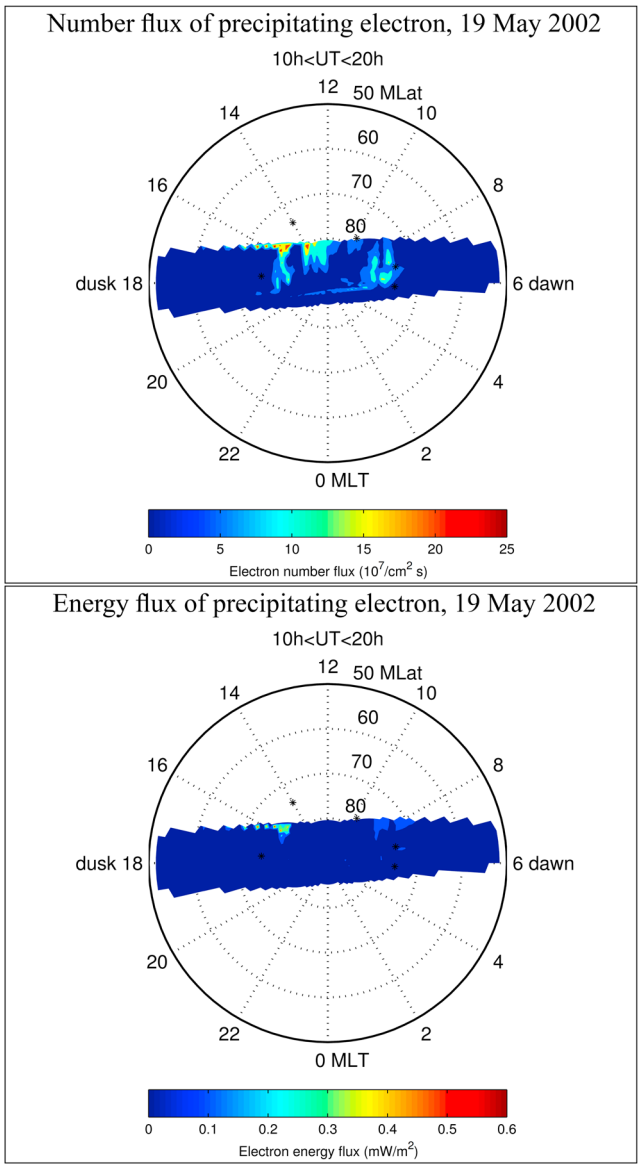

Figure 13. The number flux and energy flux of precipitating electron along successive polar DMSP orbits in the Northern Hemisphere during the radial IMF period from 10 to 20 UT.

Joule heating [e.g. *Lu et al.*, 1995b]. The energy carried by the downward Poynting flux might heat both the ionosphere and thermosphere though Joule heating. Although there are no electric field data from CHAMP, one can speculate that in between the strong FACs pair the electric field should direct toward equatorward (sunward), because the upward FACs close to the downward pair at poleward through Pedersen current. The transverse magnetic field deviations are mainly caused by FACs, which is westward directed. Therefore, the Poynting flux ($E \times B$) should point downward into the ionosphere. The soft electron precipitations can deposit energy directly at *F* region through collisions [*Fontheim et al.*, 1987], and they can increase the ionization and conductivity to raise Joule heating at higher altitude [*Carlson et al.*, 2012]. The polar MLT and MLAT distribution of the number and energy flux of precipitating electrons from DMSP F13 during 10–20 UT periods has been shown in Figure 13. It is interesting to see that there are large number fluxes of precipitating electrons with low-energy fluxes in the cusp region, which might indicate that there are strong soft electron precipitations in the norther cusp region. In the present study we can not quantify the effects of different heating processes on the enhancement of the neutral mass density, but previous model work has investigated the relative importance of different heating mechanism theoretically [*Deng et al.*, 2013]. They have found that both Poynting flux and soft electron precipitation are important in producing neutral

density enhancement near 400 km altitude and combined effects can cause more than 50% increased neutral density.

Although the geomagnetic activity indices (*AE*, *DST*, and CPCP) are found to be generally at low levels during periods of radial IMF [e.g., *Farrugia et al.*, 2007; *Shue et al.*, 2009; *Farrugia et al.*, 2010], the ionosphere and thermosphere in the cusp region are active in our case in the Northern Hemisphere. Obvious hemispheric and local time asymmetries have been disclosed.

5. Summary

In this study we have analyzed an interval on 19 May 2002 when there is a long period of strong radial IMF lasting for 10 h with a constant cone angle of about 160°. We have used the high-resolution CHAMP FGM vector magnetic field data to investigate the characteristics of FACs. Plasma data from the DMSP F13 satellite have been used to investigate the associated plasma convection flow and upflow. Additionally, the temporal response of the thermospheric air density is investigated. The geomagnetic indices are at low levels with *DST* of about −40 nT and *AE* about 100 nT on average. The cross polar cap potential output by Assimilative Mapping of Ionospheric Electrodynamics and from DMSP observations are also weak, with an average value of 15–20 kV. However, obvious dayside-nightside and interhemispheric asymmetries have been disclosed in the ionospheric and thermospheric responses. In the southern polar region both FACs and air densities are generally weak, and the convection cells stay in the two-cell structure. The southern ionosphere and thermosphere remain calm. However, there are obvious activities in the northern cusp region. The cusp FACs keep strong in intensity after the preceding storm time. The sunward flows in excess of 700 m/s occur in the cusp region. An aurora spot is observed in the northern cusp region while not in the south. These ionospheric features might be manifestations of magnetic merging occurring only in the poleward region of the northern cusp. These may form during earthward radial IMF conditions in connection with the geomagnetic field orientation on the flanks, satisfying the antiparallel merging paradigm. The upwelling of neutral gas related to the enhanced FAC pairs occur in the cusp region, which subsequently propagate equatorward on the dayside. The present study demonstrates that there can be significant energy deposition in the cusp region from the magnetosphere into the ionosphere and thermosphere during radial IMF periods.

Acknowledgements

The operational support of the CHAMP mission by the German Aerospace Center (DLR) and the financial support for the data processing by the Federal Ministry of Education (BMBF), as part of the Geotechnology Programme, are gratefully acknowledged. We thank the Center for Space Sciences at the University of Texas at Dallas and the US Air Force for providing the DMSP IDM plasma data and the Space Physics Interactive Data Resource (SPIDR) for providing the DMSP SSJ/4 data. The WDC C2 for Geomagnetism at Kyoto are greatly acknowledged for providing the geomagnetic indices data. This work is supported by the National Nature Science Foundation of China (40974096 and 41222030), Program for Young Top Talents by the Organization Department of China, Program for New Century Excellent Talents in University by the Ministry of Education, and the Specialized Research Fund for State Key Laboratories. The work of JS and GP was partially supported by grant NSC-102-2111-M-008-017 to National Central University.

Alan Rodger thanks the reviewers for their assistance in evaluating this paper.

References

Amata, E., S. P. Savin, D. Ambrosino, Y. V. Bogdanova, M. F. Marcucci, S. Romanov, and A. Skalsky (2011), High kinetic energy density jets in the Earth's magnetosheath: A case study, *Planet. Space Sci.*, *59*, 482–494, doi:10.1016/j.pss.2010.07.021.

Anderson, B. J., K. Takahashi, T. Kamei, C. L. Waters, and B. A. Toth (2002), Birkeland current system key parameters derived from Iridium observations: Method and initial validation results, *J. Geophys. Res.*, *107*(A6), 1079, doi:10.1029/2001JA000080.

Bythrow, P. F., T. A. Potemra, and L. J. Zanetti (1984), Variation of the auroral Birkeland and current pattern associated with the north-south component of the IMF, in *Magnetospheric Currents*, pp. 131–136, AGU, Washington, D. C.

Carlson, H. C., T. Spain, A. Aruliah, A. Skjaeveland, and J. Moen (2012), First-principles physics of cusp/polar cap thermospheric disturbances, *Geophys. Res. Lett.*, *39*, L19103, doi:10.1029/2012GL053034.

Cassak, P. A. (2011), Theory and simulations of the scaling of magnetic reconnection with symmetric shear flow, *Phys. Plasmas*, *18*(7), 072106, doi:10.1063/1.3602859.

Cattell, C., J. Dombeck, W. Peria, R. Strangeway, R. Elphic, and C. Carlson (2003), Fast Auroral Snapshot observations of the dependence of dayside auroral field-aligned currents on solar wind parameters and solar illumination, *J. Geophys. Res.*, *108*(A3), 1112, doi:10.1029/2001JA000321.

Clauer, C. R., and E. Friis-Christensen (1988), High-latitude dayside electric fields and currents during strong northward interplanetary magnetic field—Observations and model simulation, *J. Geophys. Res.*, *93*, 2749–2757.

Cowley, S. W. H. (1981), Asymmetry effects associated with the X-component of the IMF in a magnetically open magnetosphere, *Planet. Space Sci.*, *29*, 809–818, doi:10.1016/0032-0633(81)90071-4.

Crooker, N. U. (1979), Dayside merging and cusp geometry, *J. Geophys. Res.*, *84*, 951–959, doi:10.1029/JA084iA03p00951.

Crooker, N. U. (1988), Mapping the merging potential from the magnetopause to the ionosphere through the dayside cusp, *J. Geophys. Res.*, *93*, 7338–7344.

Crowley, G., D. J. Knipp, K. A. Drake, J. Lei, E. Sutton, and H. Lühr (2010), Thermospheric density enhancements in the dayside cusp region during strong B_Y conditions, *Geophys. Res. Lett.*, *37*, L07110, doi:10.1029/2009GL042143.

Deng, Y., T. J. Fuller-Rowell, A. J. Ridley, D. Knipp, and R. E. Lopez (2013), Theoretical study: Influence of different energy sources on the cusp neutral density enhancement, *J. Geophys. Res. Space Physics*, *118*, 2340–2349, doi:10.1002/jgra.50197.

Dmitriev, A. V., J. K. Chao, and D. J. Wu (2003), Comparative study of bow shock models using Wind and Geotail observations, *J. Geophys. Res.*, *108*(A12), 1464, doi:10.1029/2003JA010027.

Doornbos, E. v. d. I., H. Lühr, M. Förster, and G. Koppenwallner (2010), Neutral density and crosswind determination from arbitrarily oriented multiaxis accelerometers on satellites, *J. Spacecr. Rock.*, *47*, 580–589, doi:10.2514/1.48114.

Dungey, J. W. (1963), The structure of the exosphere or adventures in velocity space, in *Geophysics, The Earth's Environment*, edited by C. DeWitt, J. Hieblot, and A. Lebeau, Gordon and Breach, New York.

Eriksson, S., and L. Rastätter (2013), Alfvén Mach number and IMF clock angle dependencies of sunward flow channels in the magnetosphere, *Geophys. Res. Lett.*, *40*, 1257–1262, doi:10.1002/grl.50307.

Eriksson, S., M. R. Hairston, F. J. Rich, H. Korth, Y. Zhang, and B. J. Anderson (2009), High-latitude ionosphere convection and Birkeland current response for the 15 May 2005 magnetic storm recovery phase, *J. Geophys. Res.*, *113*, A00A08, doi:10.1029/2008JA013139.

Erlandson, R. R., L. J. Zanetti, T. A. Potemra, P. F. Bythrow, and R. Lundin (1988), IMF By dependence of region 1 Birkeland currents near noon, *J. Geophys. Res.*, *93*, 9804–9814.
Fairfield, D. H., W. Baumjohann, G. Paschmann, H. Luehr, and D. G. Sibeck (1990), Upstream pressure variations associated with the bow shock and their effects on the magnetosphere, *J. Geophys. Res.*, *95*, 3773–3786, doi:10.1029/JA095iA04p03773.
Farrugia, C. J., A. Grocott, P. E. Sandholt, S. W. H. Cowley, Y. Miyoshi, F. J. Rich, V. K. Jordanova, R. B. Torbert, and A. Sharma (2007), The magnetosphere under weak solar wind forcing, *Ann. Geophys.*, *25*, 191–205, doi:10.5194/angeo-25-191-2007.
Farrugia, C. J., et al. (2010), Magnetosheath for almost-aligned solar wind magnetic field and flow vectors: Wind observations across the dawnside magnetosheath at X = −12 Re, *J. Geophys. Res.*, *115*, A08227, doi:10.1029/2009JA015128.
Feldshtein, I. I., and A. E. Levitin (1986), Solar wind control of electric fields and currents in the ionosphere, *J. Geomagn. Geoelec.*, *38*, 1143–1182.
Fontheim, E. G., L. H. Brace, and J. D. Winningham (1987), Properties of low-energy electron precipitation in the cleft during periods of unusually high ambient electron temperatures, *J. Geophys. Res.*, *92*, 12,267–12,273, doi:10.1029/JA092iA11p12267.
Friis-Christensen, E., Y. Kamide, A. D. Richmond, and S. Matsushita (1985), Interplanetary magnetic field control of high-latitude electric fields and currents determined from Greenland magnetometer data, *J. Geophys. Res.*, *90*, 1325–1338.
Fujii, R., and T. Iijima (1987), Control of the ionospheric conductivities on large-scale Birkeland current intensities under geomagnetic quiet conditions, *J. Geophys. Res.*, *92*, 4505–4513, doi:10.1029/JA092iA05p04505.
Fujii, R., H. Fukunishi, S. Kokubun, M. Sugiura, F. Tohyama, H. Hayakawa, K. Tsuruda, and T. Okada (1992), Field-aligned current signatures during the March 13–14, 1989, great magnetic storm, *J. Geophys. Res.*, *97*, 10,703–10,715, doi:10.1029/92JA00171.
Gjerloev, J. W., S. Ohtani, T. Iijima, B. Anderson, J. Slavin, and G. Le (2011), Characteristics of the terrestrial field-aligned current system, *Ann. Geophys.*, *29*, 1713–1729, doi:10.5194/angeo-29-1713-2011.
Green, D. L., C. L. Waters, B. J. Anderson, and H. Korth (2009), Seasonal and interplanetary magnetic field dependence of the field-aligned currents for both Northern and Southern Hemispheres, *Ann. Geophys.*, *27*, 1701–1715, doi:10.5194/angeo-27-1701-2009.
Haraguchi, K., H. Kawano, K. Yumoto, S. Ohtani, T. Higuchi, and G. Ueno (2004), Ionospheric conductivity dependence of dayside region 0, 1, and 2 field aligned current systems, *Ann. Geophys.*, *22*, 2775–2783.
Hardy, D. A., L. K. Schmitt, M. S. Gussenhoven, F. J. Marshall, and H. C. Yeh (1984), Precipitating electron and ion detectors (SSJ/4) for the block 5D/Flights 6-10 DMSP (Defense Meteorological Satellite Program) satellites: Calibration and data presentation, *Rep. AFGL-TR-84-0314*, Air Force Geophys. Lab., Air Force Base, Mass.
He, M., J. Vogt, H. Lühr, E. Sorbalo, A. Blagau, G. Le, and G. Lu (2012), A high-resolution model of field-aligned currents through empirical orthogonal functions analysis (MFACE), *Geophys. Res. Lett.*, *39*, L18105, doi:10.1029/2012GL053168.
Heelis, R. A., J. D. Winningham, M. Sugiura, and N. C. Maynard (1984), Particle acceleration parallel and perpendicular to the magnetic field observed by DE-2, *J. Geophys. Res.*, *89*, 3893–3902, doi:10.1029/JA089iA06p03893.
Hietala, H., T. V. Laitinen, R. Vainio, A. Vaivads, M. Palmroth, T. I. Pulkkinen, H. E. J. Koskinen, E. A. Lucek, and H. Reme (2009), Supermagnetosonic jets behind a collisionless quasiparallel shock, *Phys. Rev. Lett.*, *103*, 245001.
Hietala, H., N. Partamies, T. V. Laitinen, L. B. N. Clausen, G. Facskó, A. Vaivads, H. E. J. Koskinen, I. Dandouras, H. Réme, and E. A. Lucek (2012), Supermagnetosonic subsolar magnetosheath jets and their effects: From the solar wind to the ionospheric convection, *Ann. Geophys.*, *30*, 33–48, doi:10.5194/angeo-30-33-2012.
Holzworth, R. H., and C.-I. Meng (1975), Mathematical representation of the auroral oval, *Geophys. Res. Lett.*, *2*, 377–380, doi:10.1029/GL002i009p00377.
Iijima, T., and T. Potemra (1976), Field-aligned currents in the dayside cusp observed by Triad, *J. Geophys. Res.*, *81*, 5971–5979.
Iijima, T., T. A. Potemra, L. J. Zanetti, and P. F. Bythrow (1984), Large-scale Birke-land currents in the dayside polar region during strongly northward IMF: Anew Birkeland current system, *J. Geophys. Res.*, *89*, 7441–7452.
Juusola, L., K. Kauristie, O. Amm, and P. Ritter (2009), Statistical dependence of auroral ionospheric currents on solar wind and geomagnetic parameters from 5 years of CHAMP satellite data, *Ann. Geophys.*, *27*, 1005–1017, doi:10.5194/angeo-27-1005-2009.
Kan, J. R., and L. C. Lee (1979), Energy coupling function and solar wind-magnetosphere dynamo, *Geophys. Res. Lett.*, *6*, 577–580.
Kervalishvili, G. N., and H. Lühr (2014), Climatology of zonal wind and large-scale FAC with respect to the density anomaly in the cusp region: Seasonal, solar cycle, and IMF By dependence, *Ann. Geophys.*, *32*, 249–261, doi:10.5194/angeo-32-249-2014.
Knipp, D., S. Eriksson, L. Kilcommons, G. Crowley, J. Lei, M. Hairston, and K. Drake (2011), Extreme Poynting flux in the dayside thermosphere: Examples and statistics, *Geophys. Res. Lett.*, *38*, L16102, doi:10.1029/2011GL048302.
Lavraud, B., and J. E. Borovsky (2008), Altered solar wind-magnetosphere interaction at low Mach numbers: Coronal mass ejections, *J. Geophys. Res.*, *113*, A00B08, doi:10.1029/2008JA013192.
Li, W., D. Knipp, J. Lei, and J. Raeder (2011), The relation between dayside local Poynting flux enhancement and cusp reconnection, *J. Geophys. Res.*, *116*, A08301, doi:10.1029/2011JA016566.
Lin, Y., and X. Y. Wang (2005), Three-dimensional global hybrid simulation of dayside dynamics associated with the quasi-parallel bow shock, *J. Geophys. Res.*, *110*, A12216, doi:10.1029/2005JA011243.
Lu, G., L. R. Lyons, P. H. Reiff, W. F. Denig, O. de la Beaujardiere, H. W. Kroehl, P. T. Newell, F. J. Rich, H. Opgenoorth, and M. A. L. Persson (1995a), Characteristics of ionospheric convection and field-aligned current in the dayside cusp region, *J. Geophys. Res.*, *100*, 11,845–11,861, doi:10.1029/94JA02665.
Lu, G., A. D. Richmond, B. A. Emery, and R. G. Roble (1995b), Magnetosphere-ionosphree-thermosphere coupling: Effect of neutral winds on energy transfer and field-aligned current, *J. Geophys. Res.*, *100*, 19,643–19,659, doi:10.1029/95JA00766.
Lühr, H., J. Warnecke, and M. K. A. Rother (1996), An algorithm for estimating field-aligned currents from single spacecraft magnetic field measurements: A diagnostic tool applied to Freja satellite data, *IEEE Trans. Geosci. Remote Sens.*, *34*, 1369–1376.
Lühr, H., M. Rotter, W. Köhler, P. Ritter, and L. Grunwaldt (2004), Thermospheric up-welling in the cusp region: Evidence from CHAMP observations, *Geophys. Res. Lett.*, *31*, L06805, doi:10.1029/2003GL019314.
McDiarmid, I. B., J. R. Burrows, and M. D. Wilson (1979), Large-scale magnetic field perturbations and particle measurements at 1400 km on the dayside, *J. Geophys. Res.*, *84*, 1431–1441.
Mei, Y., N. U. Crooker, and G. L. Siscoe (1994), Cusp current modeling: A systematic approach, *J. Geophys. Res.*, *99*, 4027–4038.
Merka, J., A. Szabo, J. Šafránková, and Z. Němeček (2003), Earth's bow shock and magnetopause in the case of a field-aligned upstream flow: Observation and model comparison, *J. Geophys. Res.*, *108*(A7), 1269, doi:10.1029/2002JA009697.
Nenovski, P. (2009), Comparison of simulated and observed large-scale, field-aligned current structures, *Ann. Geophys.*, *26*, 281–293.
Neugebauer, M., and R. Goldstein (1997), Particle and field signatures of coronal mass ejections in the solar wind, in *Coronal Mass Ejections, Geophys. Monogr. Ser.*, vol. 99, edited by N. Crooker, J. A. Joselyn, and J. Feynman, pp. 245–251, AGU, Washington D. C. doi:10.1029/GM099p0245.

Němeček, Z., J. Šafránková, L. Přech, D. G. Sibeck, S. Kokubun, and T. Mukai (1998), Transient flux enhancements in the magnetosheath, *Geophys. Res. Lett.*, *25*, 1273–1276, doi:10.1029/98GL50873.
Omidi, N., D. G. Sibeck, and X. Blanco-Cano (2009), Foreshock compressional boundary, *J. Geophys. Res.*, *114*, A08205, doi:10.1029/2008JA013950.
Papitashvili, V. O., and F. J. Rich (2002), High-latitude ionospheric convection models derived from Defense Meteorological Satellite Program ion drift observations and parameterized by the interplanetary magnetic field strength and direction, *J. Geophys. Res.*, *107*(A8), SIA 17-1–SIA 17-13, doi:10.1029/2001JA000264.
Parker, E. N. (1958), Dynamics of the interplanetary gas and magnetic fields, *Astrophys. J.*, *128*, 664, doi:10.1086/146579.
Potemra, T. A., L. J. Zanetti, R. E. Erlandson, P. F. Bythrow, G. Gustafsson, and M. H. Acuna (1987), Observations of large-scale Birkeland currents with Viking, *Geophys. Res. Lett.*, *14*, 419–422.
Reiff, P. H., and J. L. Burch (1985), IMF B_y-dependent plasma flow and birkland currents in the dayside magnetosphere: 2. A global model for northward and southward IMF, *J. Geophys. Res.*, *90*, 1595–1609.
Reigber, C., H. Lühr, and P. Schwintzer (2002), CHAMP mission status, *Adv. Space Res.*, *30*, 129–134.
Rich, F. J., and M. Hairston (1994), Large-scale convection patterns observed by DMSP, *J. Geophys. Res.*, *99*, 3827–3844.
Richmond, A. D. (1995), Ionospheric electrodynamics using magnetic Apex coordinates, *J. Geophys. Res.*, *47*, 191–212.
Ridley, A. J. (2005), A new formulation for the ionospheric cross polar cap potential including saturation effects, *Ann. Geophys.*, *23*, 3533–3547.
Ridley, A. J., T. I. Gombosi, and D. L. DeZeeuw (2004), Ionospheric control of the magnetosphere: Conductance, *Ann. Geophys.*, *22*, 567–584.
Robinson, R. M., R. R. Vondrak, K. Miller, T. Dabbs, and D. A. Hardy (1987), On calculating ionospheric conductances from the flux and energy of precipitating electrons, *J. Geophys. Res.*, *92*(A3), 2565–2569.
Russell, C. T., and M. Fleishman (2002), Joint control of region-2 field-aligned currents by the east-west component of the interplanetary electric field and polar cap illumination, *J. Atmos. Terr. Phys.*, *64*, 1803–1808, doi:10.1016/S1364-6826(02)00189-X.
Russell, C. T., S. M. Petrinec, T. L. Zhang, P. Song, and H. Kawano (1997), The effect of foreshock on the motion of the dayside magnetopause, *Geophys. Res. Lett.*, *24*, 1439–1441, doi:10.1029/97GL01408.
Shue, J.-H., P. T. Newell, K. Liou, C.-I. Meng, and S. W. H. Cowley (2002), Interplanetary magnetic field B_x asymmetry effect on auroral brightness, *J. Geophys. Res.*, *107*(A8), 1197, doi:10.1029/2001JA000229.
Shue, J.-H., J.-K. Chao, P. Song, J. P. McFadden, A. Suvorova, V. Angelopoulos, K. H. Glassmeier, and F. Plaschke (2009), Anomalous magnetosheath flows and distorted subsolar magnetopause for radial interplanetary magnetic fields, *Geophys. Res. Lett.*, *36*, L18112, doi:10.1029/2009GL039842.
Stauning, P. (2002), Field-aligned ionospheric current systems observed from Magsat and Oersted satellites during northward IMF, *Geophys. Res. Lett.*, *29*(15), 8005, doi:10.1029/2001GL013961.
Strangeway, R. J., C. T. Russell, C. W. Carlson, J. P. McFadden, R. E. Ergun, M. Temerin, D. M. Klumpar, W. K. Peterson, and T. E. Moore (2000), Cusp field-aligned currents and ion outflows, *J. Geophys. Res.*, *105*, 21,129–21,141, doi:10.1029/2000JA900032.
Strangeway, R. J., R. E. Ergun, Y.-J. Su, C. W. Carlson, and R. C. Elphic (2005), Factors controlling ionospheric outflows as observed at intermediate altitudes, *J. Geophys. Res.*, *110*, A03221, doi:10.1029/2004JA010829.
Suvorova, A. V., J.-H. Shue, A. V. Dmitriev, D. G. Sibeck, J. P. McFadden, H. Hasegawa, K. Ackerson, K. Jelínek, J. Šafránková, and Z. Němeček (2010), Magnetopause expansions for quasi-radial interplanetary magnetic field: THEMIS and Geotail observations, *J. Geophys. Res.*, *115*, A10216, doi:10.1029/2010JA015404.
Taguchi, S., M. Sugiura, J. D. Winningham, and J. A. Slavin (1993), Characterization of the IMF By-dependent field-aligned currents in the cleft region based on DE 2 observations, *J. Geophys. Res.*, *98*, 1393–1407.
Tang, B. B., C. Wang, and W. Y. Li (2013), The magnetosphere under the radial interplanetary magnetic field: A numerical study, *J. Geophys. Res. Space Physics*, *118*, 7674–7682, doi:10.1002/2013JA019155.
Verigin, M., G. Kotova, A. Szabo, J. Slavin, T. Gombosi, K. Kabin, F. Shugaev, and A. Kalinchenko (2001), Wind observations of the terrestrial bow shock: 3-D shape and motion, *Earth Planets Space*, *53*, 1001–1009.
Wang, H., H. Lühr, and S. Y. Ma (2005), Solar zenith angle and merging electric field control of field-aligned currents: A statistical study of the Southern Hemisphere, *J. Geophys. Res.*, *110*, A03306, doi:10.1029/2004JA010530.
Wang, H., H. Lühr, S. Y. Ma, J. Weygand, and R. M. Skoug (2006), Field-aligned currents observed by CHAMP during the intense 2003 geomagnetic storm events, *Ann. Geophys.*, *24*, 311–324.
Wang, H., A. J. Ridley, and H. Lühr (2008a), SWMF simulation of field-aligned currents for a varying northward and duskward IMF with nonzero dipole tilt, *Ann. Geophys.*, *26*, 1461–1477, doi:10.5194/angeo-26-1461-2008.
Wang, H., A. J. Ridley, H. Lühr, M. W. Liemohn, and S. Y. Ma (2008b), Statistical study of the subauroral polarization stream: Its dependence on the cross-polar cap potential and subauroral conductance, *J. Geophys. Res.*, *113*, A12311, doi:10.1029/2008JA013529.
Watanabe, M., T. Iijima, and F. J. Rich (1996), Synthesis models of dayside field-aligned currents for strong interplanetary magnetic field By, *J. Geophys. Res.*, *101*, 13,303–13,320, doi:10.1029/96JA00482.
Watari, S., M. Vandas, and T. Watanabe (2005), Solar cycle variation of long-duration radial interplanetary magnetic field events at 1 AU, *J. Geophys. Res.*, *110*, A12102, doi:10.1029/2005JA011165.
Weimer, D. R. (2001), Maps of ionospheric field-aligned currents as a function of the interplanetary magnetic field derived from Dynamics Explorer 2 data, *J. Geophys. Res.*, *106*, 12,889–12,902, doi:10.1029/2000JA000295.
Wilder, F. D., S. Eriksson, H. Korth, J. B. H. Baker, M. R. Hairston, C. Heinselman, and B. J. Anderson (2013), Field-aligned current reconfiguration and magnetospheric response to an impulse in the interplanetary magnetic field B_Y component, *Geophys. Res. Lett.*, *40*, 2489–2494, doi:10.1002/grl.50505.
Wilhjelm, J. E., E. Friis-Christensen, and T. A. Potemra (1978), The relationship between ionospheric and field-aligned currents in the dayside cusp, *J. Geophys. Res.*, *83*, 5586–5592.
Wing, S., S.-I. Ohtani, P. T. Newell, T. Higuchi, G. Ueno, and J. M. Weygand (2010), Dayside field-aligned current source regions, *J. Geophys. Res.*, *115*, A12215, doi:10.1029/2010JA015837.
Xu, D., and M. G. Kivelson (1994), Polar cap field-aligned currents for southward interplanetary magnetic fields, *J. Geophys. Res.*, *99*, 6067–6078, doi:10.1029/93JA02697.
Yamauchi, M., R. Lundin, and J. Woch (1993), The interplanetary magnetic field By effects on large-scale field-aligned currents near local noon—Contributions from cusp part and noncusp part, *J. Geophys. Res.*, *98*, 5761–5767.
Yang, Y. F., J. Y. Lu, J.-S. Wang, Z. Peng, and L. Zhou (2013), Influence of interplanetary magnetic field and solar wind on auroral brightness in different regions, *J. Geophys. Res. Space Physics*, *118*, 209–217, doi:10.1029/2012JA017727.